Deciphering the mechanism of the Ni-photocatalyzed C–O cross-coupling reaction using a tridentate pyridinophane ligand

Hanah Na[†] and Liviu M. Mirica[†,*]

[†]Department of Chemistry, University of Illinois at Urbana-Champaign, 600 S. Mathews Avenue, Urbana, Illinois, 61801

*mirica@illinois.edu

KEYWORDS. Photocatalysis, cross-coupling reactions, organometallic chemistry, nickel, tridentate ligands, electron paramagnetic resonance

Abstract

Photoredox nickel catalysis has emerged as a powerful strategy for cross-coupling reactions. Although the involvement of paramagnetic Ni(I)/Ni(III) species as active intermediates in the catalytic cycle has been proposed, a thorough spectroscopic investigation of these species is lacking. Herein, we report a new class of tridentate pyridinophane ligands ^{R}N3 that allow for detailed mechanistic studies of the photocatalytic C–O coupling reaction. The derived (^{R}N3)Ni complexes are active catalysts under mild conditions and without an additional photocatalyst. We also provide direct evidence for the key steps involving paramagnetic Ni species in the proposed catalytic cycle: the oxidative addition of an aryl halide to a Ni(I) species, the ligand exchange/transmetalation at a Ni(III) center, and the C–O reductive elimination from a Ni(III)

species. Overall, the present work suggests the ^{R}N3 ligands are a practical platform for mechanistic studies of Ni-catalyzed reactions and for the development of new catalytic applications.

Introduction

The carbon–oxygen (C–O) bond-forming reactions are of particular interest in the field of organic synthesis, as C–O bonds are prevalent in many natural products, pharmaceuticals, and agrochemicals.[1-3] Although Pd-based C–O cross-coupling catalysts are well established,[4-7] there has been a great interest in developing sustainable catalytic systems based on earth-abundant nickel. In this regard, photoredox/nickel dual catalysis and light-promoted Ni catalysis have emerged as powerful strategies for challenging C–O bond formations.[8-11] Accordingly, an in-depth mechanistic understanding of Ni-mediated photocatalysis is essential for rational reaction design and optimization. From a mechanistic viewpoint, while the photocatalytic cycle is well-understood, the Ni-mediated redox cycle remains elusive as intermediates in various oxidation states (from Ni^{0} to Ni^{IV}) have been proposed.[12] For example, the involvement of paramagnetic Ni^{I} and Ni^{III} species has been commonly implicated, yet such intermediates have not been thoroughly investigated, and the key catalytic steps of oxidative addition, transmetalation, and reductive elimination have rarely been observed directly.[10,13,14]

Our group has employed tetradentate azamacrocycle *N*,*N*'-dialkyl-2,11-diaza[3.3](2,6)pyridinophanes (^{R}N4) ligands to isolate and characterize Ni^{III} species capable of C–C[15-18] and C–heteroatom[15,19,20] bond formation reactions, and to probe the involvement of high-valent Ni species in these reactions. However, considering that the most ubiquitous ligands in Ni cross-coupling and photocatalytic reactions are the bidentate bipyridine ligands,[8-11,21] the ^{R}N4

ligands were thought to be less effective ligands owing to the crowded environment around the Ni center, which is also expected to disfavor the formation of Ni^{I} species. By contrast, a bidentate ligand structure is not suitable for stabilizing high-valent Ni species, thus hampering the investigation of such Ni intermediates.[22] Considering these aspects, we sought to identify an optimal ligand framework positioned in between bipyridine and ^{R}N4 ligands in terms of denticity, molecular structure, and functionality, and thus the pyridinophane tridentate ^{R}N3 ligands were targeted (Fig. 1a). These ^{R}N3 ligands are structurally analogous to the ^{R}N4 ligands, possessing a rigid aromatic pyridinophane framework and containing only one flexible chelating arm that allows for either a κ^2 or κ^3 coordination. Surprisingly, such ^{R}N3 ligands have never been synthesized to date, likely due to the lack of an efficient synthetic route. Several other well-known *fac*-capping tridentate N-donor ligands such as tris(pyrazoyl)borate (Tp^{-}),[22] tris(pyrazolyl)methane (Tpm),[23] or 1,4,7-trimethyl-1,4,7-triazacyclononane (Me_3TACN, Fig. 1b)[24] have been reported, yet these systems were shown to only stabilize high-valent Ni species.

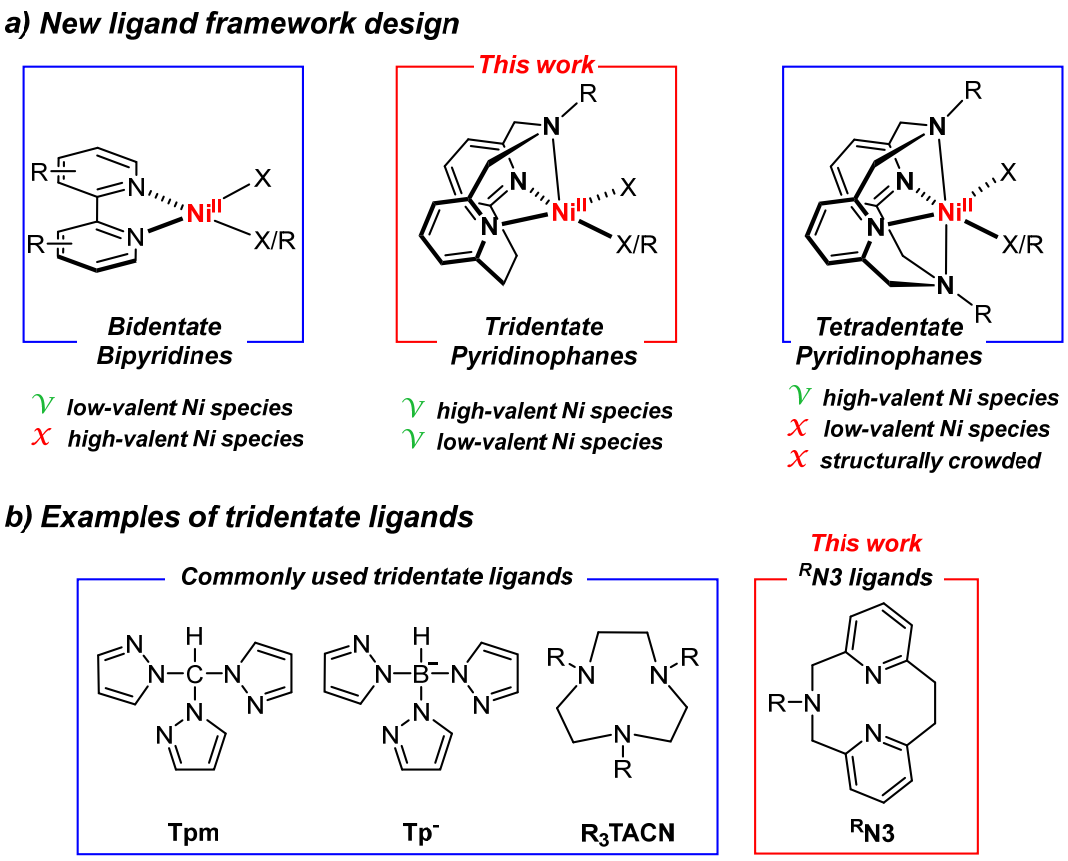

Figure 1. (a) New ligand framework design. (b) Representative tridentate N-donor ligands commonly used for stabilizing uncommon Ni oxidation states and the newly developed tridentate ligand developed in this work.

In this work, we report the development of new *N*-alkyl-2-aza[3.2](2,6)pyridionphanes (^{R}N3, R = Me or ^{i}Pr) ligands, which embody our design criteria for photocatalytic applications and mechanistic studies. The corresponding (^{R}N3)Ni complexes are active C–O cross-coupling catalysts upon light excitation and without an added precious-metal photocatalyst. Importantly, we show that the utilization of the tridentate ^{R}N3 ligands allows for a comprehensive examination of the Ni intermediates proposed in the individual steps of the cross-coupling catalytic cycle: oxidative addition, transmetalation/ligand exchange, and reductive elimination, all these steps

involving paramagnetic Ni^{I} or Ni^{III} species.

Results and discussion

Ligand Development

In 1958, Overberger et al. reported the reduction of N-nitrosodibenzylamines by $Na_2S_2O_4$ to generate the hydrocarbon product with evolution of N_2.[25] However, this reaction has received little attention since then, and only one report by Takemura et al. in 1988 exploited the *N*-nitroso reduction reaction to obtain [2.2]cyclophane derivatives.[26] We speculated that this N-extrusion reaction would provide an efficient synthetic pathway for tridentate pyridinophane ligands. Our synthesis starts with the unsymmetrical pryridinophane precursor *N*-tosyl-2,11-diaza[3.3](2,6)pyridionphane (^{TsH}N4, Fig. 2a).[27] For the nitrosylation step, ^{TsH}N4 was treated with HNO_2 to generate the *N*-nitroso intermediate ^{TsNO}N4 in 85% yield. Subsequent reductive elimination of nitrogen from the *N*-nitrosoamine was performed with $Na_2S_2O_4$ under basic conditions, converting ^{TsNO}N4 to ^{Ts}N3 in 75% yield. Additional steps of detosylation and methylation or isopropylation afforded the alkylated ligand variants ^{Me}N3 or ^{iPr}N3 in ~45% overall yields, confirming that further functionalization can be easily achieved. The *N*-nitroso reduction conditions are mild, suggesting a broad functional group tolerance. Since all reaction steps do not require extensive purification and their yields are high, the development of this novel synthetic route provides an opportunity to access a variety of ligand structures by further functionalization or starting from different secondary amine precursors. Notably, Levin et al. have recently reported the development of an anomeric amide reagent for the oxidative extrusion of nitrogen from dibenzylamines via a isodiazene intermediate to yield C-C coupled products.[28] By comparison, our approach employs a reduction of the *N*-nitrosoamine intermediate and only uses simple and

commonly available reagents, and thus allowing for bis-2-picolylamines to be used as substrates.

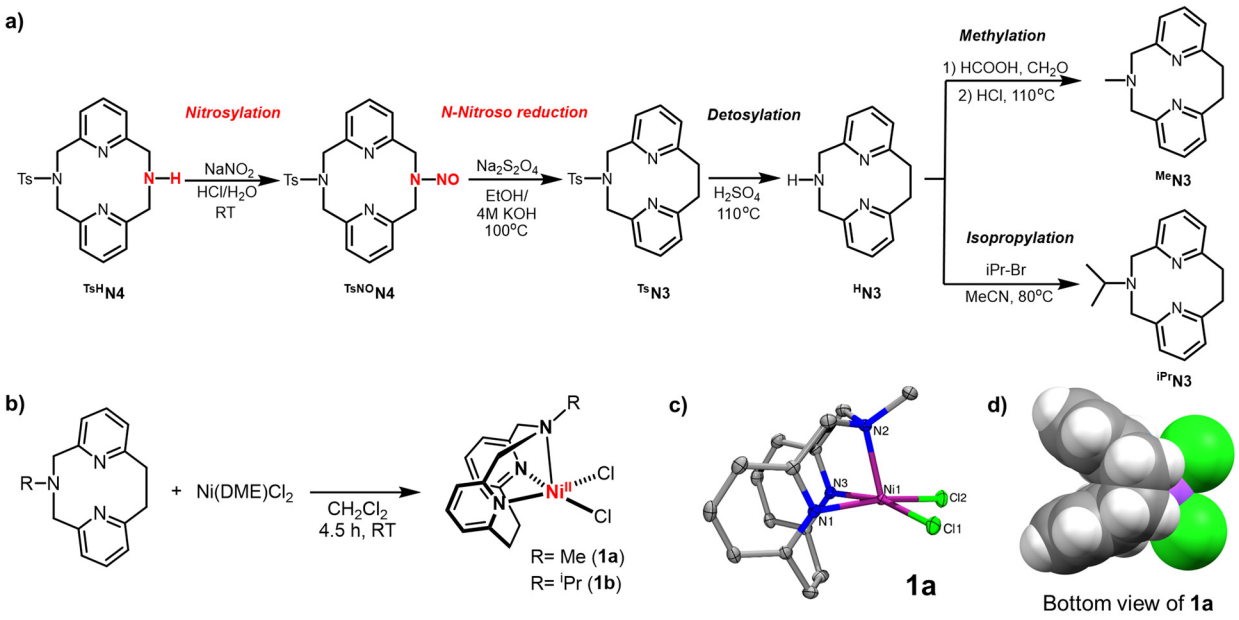

Figure 2. (a) Synthesis of newly developed ^{R}N3 type pyridinophane ligands. (b) Synthesis of (^{R}N3)NiCl$_2$ complexes (**1a** and **1b**) and (c) ORTEP representation of the **1a** obtained by X-ray diffraction (ellipsoids are shown at 50% probability and the hydrogen atoms omitted for clarity). Selected bond lengths (Å): Ni–N$_{py}$ 2.058, Ni–N$_{amine}$ 2.056, Ni–Cl 2.322. (d) Space-filling model of **1a** highlighting the steric protection of the Ni center by the H atoms of the ethylene bridge.

Synthesis and characterization of (^{R}N3)NiCl$_2$ complexes

The reaction of ^{Me}N3 or ^{iPr}N3 with Ni(DME)Cl$_2$ in CH$_2$Cl$_2$ generated the green Ni^{II}-dichloride complexes (^{Me}N3)NiCl$_2$ (**1a**) and (^{iPr}N3)NiCl$_2$ (**1b**), respectively (Fig. 2b). The molecular structures of **1a** and **1b** were determined by single crystal X-ray diffraction (Fig. 2c), to reveal similar coordination environments around the Ni center, except that the structure of **1b** exhibits slight distortions due to the bulkier ^{i}Pr substituent (Supplementary Fig. S42). The structure of **1a** reveals a five-coordinate Ni^{II} center in a square pyramidal geometry with a calculated trigonality index parameter τ of 0,[29] with an average Ni–N$_{py}$ bond length of 2.058 Å and an axial

Ni–N_{amine} bond length of 2.056 Å, which are similar to those of the related complex (^{tBu}N4)$NiCl_2$.[30] A closer look at the space-filling representation of **1a**, as shown from the bottom view and along the Ni–N_{amine} axial axis (Fig. 2d), reveals that the Ni center is sterically protected by the H atoms of the ethylene bridge and thus could lead to an increased stability of the high- or low-valent Ni intermediates (see below).

The electrochemical properties of (^{R}N3)$NiCl_2$ complexes were investigated by cyclic voltammetry (CV, Supplementary Figs. S12 and S13). The CVs of **1a** and **1b** in MeCN reveal a pseudoreversible oxidation wave at 0.71 V vs $Fc^{+/0}$, which is assigned to the $Ni^{III/II}$ couple, as well as an irreversible reduction wave at –1.20 V vs $Fc^{+/0}$ for **1a** and –1.22 V for **1b**, followed by a pseudoreversible reduction wave at –1.60 V vs $Fc^{+/0}$ for **1a** and –1.72 V for **1b**, respectively. It is important to note that the oxidation and reduction potentials for **1a** and **1b** are similar to those of (dtbbpy)$NiCl_2$, which exhibits an oxidation wave at 0.56 V vs $Fc^{+/0}$ and an irreversible reduction wave at –1.37 V vs $Fc^{+/0}$, followed by a pseudoreversible reduction wave at –1.74 V vs $Fc^{+/0}$ (Supplementary Fig. S15). By comparison, while for (^{Me}N4)$NiCl_2$ the $Ni^{III/II}$ oxidation event was observed at 0.52 V vs $Fc^{+/0}$, no reduction event was observed up to –2.00 V vs $Fc^{+/0}$,[31] supporting our hypothesis that tetradantate ligands cannot stabilize Ni^{I} species to a large extent. The accessible reduction events observed for (^{R}N3)$NiCl_2$ suggest that for these complexes the Ni^{I} oxidation state is accessible via one-electron reduction with a chemical reductant and thus it can be exploited in reactivity and mechanistic studies. When compared to (dtbbpy)$NiCl_2$, the (^{R}N3)$NiCl_2$ complexes exhibit similar oxidation and reduction potentials, which is essential for photocatalysis, yet they possess a structural advantage by containing the flexible axial amine arm that is beneficial for characterization of reaction intermediates (see below).

The UV-visible absorption spectra of **1a** and **1b** were then obtained and also analyzed computationally. The UV-vis absorption spectrum of **1a** shows an intense band around 380 nm and a less intense band around 640 nm (Fig. 3). To probe the nature of the electronic transitions, time-dependent density functional theory (TD-DFT) calculations were performed. As the ground state of **1a** has triplet spin multiplicity, the higher energy absorption feature (380 nm) is attributed to a combination of a spin-allowed Cl → ^{R}N3 ligand-to-ligand charge transfer (^{3}LLCT) and a Ni → ^{R}N3 metal-to-ligand charge transfer (^{3}MLCT), while the lower energy absorption band (640 nm) is attributed to a metal-centered (^{3}MC) d-d electronic transition (Supplementary Figs. S48–S53). The energy of the ^{3}MC d-d transition (640 nm ≈ 1.93 eV) is consistent with the electrochemical gap observed by CV (0.71 V – (–1.20 V) = 1.91 eV), further supporting that the lowest excited state (T_1) has primarily MC d-d character. For a qualitative representation of the specified transitions between the ground and excited states, we performed natural transition orbital (NTO) analysis that provides a localized picture of the transition density matrix (Fig. 3b).[32] The NTO analysis supports the assignment of the 380 nm transition to a T_n excited state with a mixed LLCT/MLCT character, while the 633 nm transition involves an electron excitation between predominantly metal-based orbitals, thus indicating a MC (d-d) transition. For 3*d* transition metal complexes, the MC (d-d) state is the lowest excited state owing to the intrinsically low ligand field strength, and the higher energy CT state and MC (d-d) state are close in energy, thus resulting in fast relaxation to the lowest-lying MC (d-d) state.[33,34] Therefore, we propose that on initial population of the MLCT/LLCT state is followed by fast relaxation to the lower MC (d-d) state with an appreciable Ni–Cl σ* orbital character (Fig. 3c), which then promotes a metal-ligand homolytic bond cleavage,[35,36] as observed recently by Doyle for a similar Ni system.[37] Since **1a**

shows a prominent absorption band at 380 nm, a purple LED lamp (λ_{max} = 390 nm) was chosen as a light source for the direct light-promoted C–O coupling reaction (see below). Finally, the UV-vis absorption spectrum and TD-DFT calculation results for **1b** are similar to those for **1a**, indicating a minimal effect of the N-substituent on the electronic structure (Supplementary Figs. S54–S59).

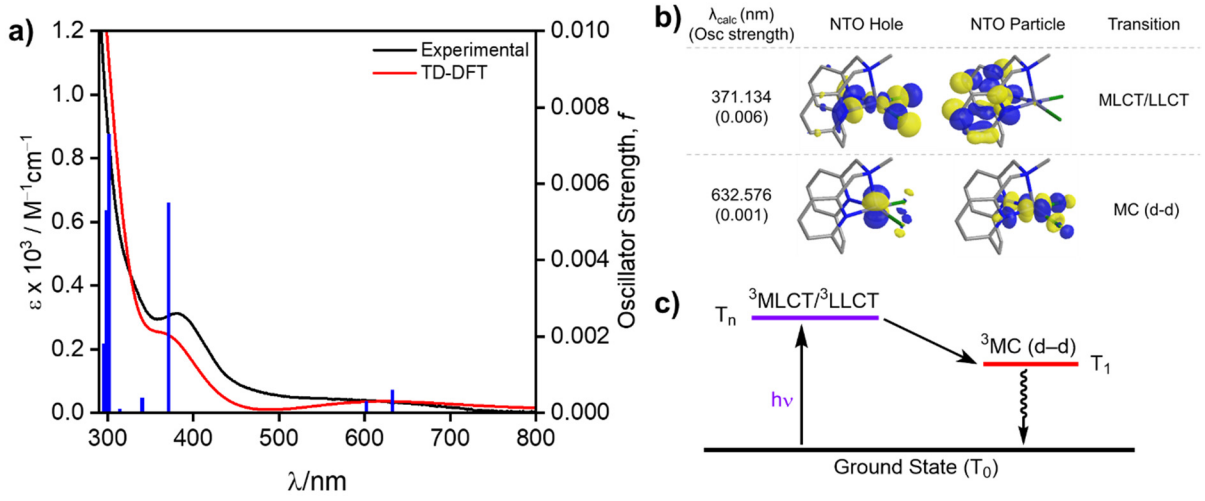

Figure 3. (a) Experimental (black line) and simulated (red line) UV-vis spectrum of **1a** with overlaid relevant oscillator strengths (solid blue bars) from TD–DFT calculations. (b) Natural transition orbitals (NTOs, 0.05 isocontour value) associated with the visible absorption bands of **1a**. (c) A simplified excited-state diagram for **1a**, showing the population of the lowest energy excited state, a ^{3}MC d-d state.

Photocatalytic C–O coupling reactions mediated by (^{R}N3)NiCl$_2$ complexes

To probe the relevance of the (^{R}N3)NiCl$_2$ complexes in photocatalysis, we evaluated their light-promoted catalytic activity in C–O cross-coupling without any additional photocatalyst. Our initial efforts focused on optimizing the reaction conditions using methanol and 4-bromoacetophenone (Table 1 and Supplementary Tables S2–S7). In the presence of 2 mol% (^{Me}N3)NiCl$_2$ (**1a**) and quinuclidine in THF, the desired C–O coupled product 4-

methoxyacetophenone was obtained in 95% yield under purple LED (λ_{max} = 390 nm) irradiation (Table 1, entry 1). Control experiments revealed that the reaction did not proceed without Ni catalyst, light, or base (Table 1, entries 2–4). The desired product was not observed when the reaction was irradiated with blue LED, suggesting the crucial role of the excitation energy (Table 1, entry 5). While inorganic bases such as K_2CO_3 were not effective, possibly due to the precipitation of halides required to stabilize the Ni^{I} intermediate[14] or the unproductive decomposition of the Ni^{III} intermediates (Supprementary Figs. S33-34), DABCO was effective but proceeded at a slightly slower rate and thus requiring a longer reaction times (Table 1, entries 6–8). Switching from **1a** to **1b** or (^{Me}N3)$NiBr_2$, lowering of catalyst loading to 0.2 mol%, or the addition of ^{Me}N3 and $Ni(DME)Cl_2$ separately instead of **1a** gave comparable yields (Table 1, entries 9–12). Notably, a 0.2 mol% catalyst loading is significantly less (~25–50 fold decrease) than the loadings used in other Ni-photocatalyzed C–O cross-couplings.[10,11] Moreover, other alcohols such as 1-hexanol and benzyl alcohol could also be employed (Supplementary Table S7, 86–90% product yield). However, the combination of **1a** and heterogenous Zn^0 or Mn^0 without light was ineffective in our conditions, likely due to the slow electron transfer kinetics or insufficient generation of the active species during catalysis.[38,39] Finally, the (^{R}N4)$Ni^{II}Cl_2$ complex supported by the tetradentate ligand ^{Me}N4 exhibited inferior performance, validating our ligand design principle (Table 1, entry 13).

Table 1. Light-promoted Ni catalytic reaction development and optimization[a]

Entry	Variation from the standard conditions	Yield (%)
1	none	95
2	no light (dark)	0
3	no (^{Me}N3)$NiCl_2$	0
4	no base	0
5	Blue LED instead of purple LED	0
6	DABCO instead of quinuclidine, 24 h	77
7	DABCO instead of quinuclidine, 36 h	96
8	K_2CO_3 instead of quinuclidine	0
9	(^{Me}N3)$NiCl_2$ 0.2 mol% instead of 2 mol%	90
10	(^{Me}N3)$NiBr_2$ instead of ^{Me}N3$NiCl_2$	90
11	(^{iPr}N3)$NiCl_2$ instead of ^{Me}N3$NiCl_2$	82
12	^{Me}N3 (2 mol%) + Ni(DME)Cl_2 (2 mol%) instead of (^{Me}N3)$NiCl_2$	77
13	(^{Me}N4)$NiCl_2$ instead of ^{Me}N3$NiCl_2$	2

[a] Reaction conditions: In a N_2-filled glovebox, 4-bromoacetophenone (0.4 mmol, 1.0 equiv), quinuclidine (0.44 mmol, 1.1 equiv), MeOH (1.6 mmol, 4 equiv), (^{Me}N3Ni)Cl_2 (2 mol%) and a magnetic stir bar were added into 0.4 mL THF in a vial. The vial was irradiated with one purple LED lamp (52 W, 390 nm) under fan cooling. After 24 h, 1,3-benzodioxole (0.4 mmol) was added to the reaction mixture as a standard and the residue was analyzed by ^{1}H NMR and GC-FID to determine the yield of C-O coupled product.

The same C-O coupling reaction was also probed under common dual Ni/photoredox catalytic conditions using various Ir or Ru photocatalysts and blue LED light (λ_{max} = 456 nm) (Table 2). The photocatalyst screening experiments revealed that the Ir photocatalysts tested here gave the desired C–O coupled product in 80–98% yield, while the Ru catalysts showed no reactivity.

Table 2. Dual Ni/photoredox catalytic reaction optimization[a]

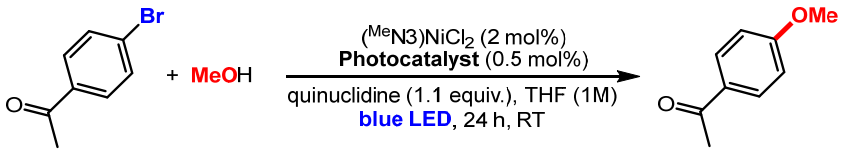

Entry	Photocatalyst	Yield (%)
1	no photocatalyst	0
2	$[Ir(dF(CF_3)_2ppy)(dtbbpy)]PF_6$	86
3	$Ir(ppy)_3$	90
4	$[Ir(ppy)_2(dtbbpy)]PF_6$	98
5	$[Ru(phen)_3]Cl_2$	~1%
6	$[Ru(bpz)_3](PF_6)_2$	0

[a] Reaction conditions: In a N_2-filled glovebox, 4-bromoacetophenone (0.4 mmol, 1.0 equiv), quinuclidine (0.44 mmol, 1.1 equiv), MeOH (1.6 mmol, 4 equiv), $(^{Me}N3)NiCl_2$ (2 mol%), photocatalyst (0.5 mol%) and a magnetic stir bar were added into 0.4 mL THF in a vial. The vial was irradiated with one blue LED lamp (50 W, 456 nm) under fan cooling. After 24 h, 1,3-benzodioxole (0.4 mmol) was added to the reaction mixture as a standard and the residue was analyzed by ^{1}H NMR and GC-FID to determine the yield of C-O coupled product.

EPR and reactivity studies

Several reports have proposed the oxidative addition of an organic halide to Ni^I to generate a Ni^{III} species is a key step in the C–O cross-coupling catalytic cycle,[13,14,37] yet minimal evidence was provided and such a step has been underexplored experimentally.[40,41] Our Ni catalysts have accessible $Ni^{II/I}$ redox potentials, thus we aimed to probe the reduction of Ni^{II} to Ni^I and the subsequent oxidative addition of an aryl halide to generate a Ni^{III} intermediate by using X-band electron paramagnetic resonance (EPR) spectroscopy. For the EPR studies, **1b** was used due to its better solubility vs **1a**. Upon the reduction of **1b** by 1 equiv decamethylcobaltocene ($CoCp^*_2$) at –95 °C (Fig. 4a), a Ni^I species **2** was formed that exhibits a rhombic EPR spectrum with $g_x = 2.241$, $g_y = 2.113$, and $g_z = 2.049$ (Fig. 4d), and suggesting the presence of a metal-based radical. When 20 equiv 4-bromoacetophenone were added to a thawing solution of **2** (Fig. 4b), the resulting EPR spectrum could be simulated with two sets of parameters corresponding to two different species in a 0.6:1 ratio and that were tentatively assigned to the initial Ni^I species and a new Ni^{III} species (Fig.

4e and Supplementary Fig. S19). We propose that the Ni^{III} species is a transient 6-coordinate (^{iPr}N3)Ni^{III}(PhAc)BrCl (**3**) complex generated through the oxidative addition of 4-bromoacetophenone to **2**. Moreover, when 40 equiv 4-bromoacetophenone were added to **2** (Fig. 4c), only a rhombic EPR signal with $g_x = 2.298$, $g_y = 2.197$, and $g_z = 2.037$ formed (Fig. 4f), which was assigned to **3** and thus strongly supporting a direct conversion from Ni^{I} (**2**) to Ni^{III} (**3**) that is promoted by the excess aryl halide. The observed EPR spectrum for **3** decays quickly upon warming up the solution for seconds at –80 °C (Supplementary Fig. S20), supporting the increased reactivity **3** and its proposed involvement in catalysis. Finally, it is important to note that to the best of our knowledge the direction observation of the oxidation addition of an aryl halide to a Ni^{I} species to generate a Ni^{III} species has not been reported to date.

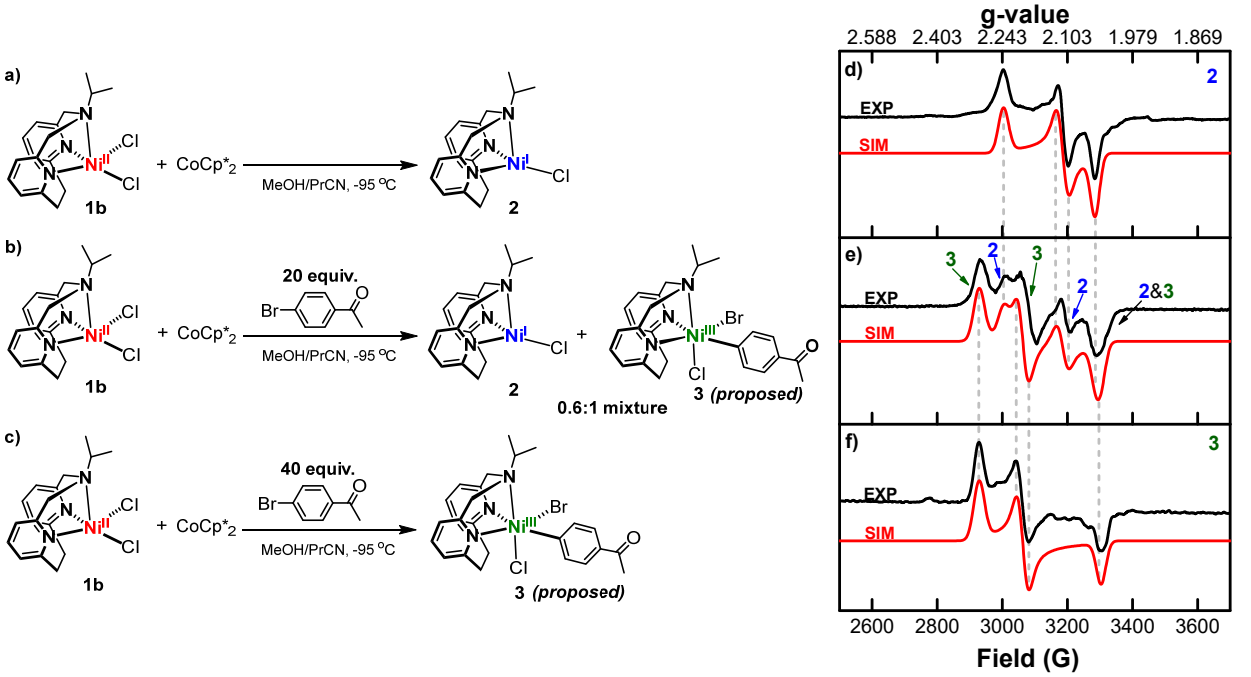

Figure 4. (left) Experimental setup for EPR detection of proposed Ni^{I} and Ni^{III} species upon reduction of **1b** and subsequent oxidative addition of aryl bromide. (right) Experimental (black)

and simulated (red) EPR spectra of the reaction mixtures recorded at 77 K in 1:5 MeOH:PrCN frozen glass: (d) **1b** + $CoCp^*_2$, (e) **1b** + $CoCp^*_2$ + 20 equiv 4-bromoacetophenone, (f) **1b** + $CoCp^*_2$ + 40 equiv 4-bromoacetophenone. The following parameters were used for simulation of (d) g_x = 2.241, g_y = 2.113, g_z = 2.049; (f) g_x = 2.298, g_y = 2.197, g_z = 2.037; (e) the simulations in (d) and (f) were added in a 0.6:1 ratio.

To further probe the role of various Ni^{III} species in the C–O coupling reaction, we independently synthesized the (^{iPr}N3)Ni^{II}(PhAc)Br complex **4** via oxidative addition of 4-bromoacetophenone to $Ni(COD)_2$ in the presence of ^{iPr}N3 (Fig. 5a). While **4** is unstable in solution at room temperature, rapidly decomposing to the green (^{iPr}N3)$Ni^{II}Br_2$ complex, it is stable at –40 °C for several hours. The decomposition of a related nickel complex, (bpy)Ni^{II}PhBr, to (bpy)$Ni^{II}Br_2$ has been observed previously and proposed to proceed via a bimolecular pathway.[42,43] The instability of **4** in solution prevented us from obtaining X-ray quality crystals, nonetheless since **4** is diamagnetic its structural evidence was provided by ^{1}H NMR obtained at –40 °C, which shows a slight peak broadening due to the flexible amine arm (Supplementary Fig. S1).[24] Oxidation of **4** with acetylferrocenium hexafluorophosphate ($^{Ac}FcPF_6$) at –40 °C generates the Ni^{III} [(^{iPr}N3)Ni^{III}(PhAc)(Br)]$^+$ complex **5** (Fig. 5a). The effective magnetic moment μ_{eff} of 1.98 μ_b, determined using the Evans method, is consistent with a S =1/2 ground state for **5**, as expected for a Ni^{III} center.[44,45] The rhombic EPR spectrum of **5** with g_x = 2.356, g_y = 2.158, g_z = 2.059 is significantly different than that of **3** (Fig. 5e vs. Fig. 4f), solidifying the proposed 6-coordinate structure in Fig. 4c. Complex **5** was stable in solution at –35 °C and can be isolated as a red solid, yet it was recalcitrant to form single crystals. Therefore, the presence of a Ni^{III} center was further confirmed by X-ray photoelectron spectroscopy (XPS), which shows an increase of the Ni $2_{p3/2}$ and $2_{p1/2}$ binding energies of ~1.5 eV for **5** versus **4**, demonstrating the presence of a further

oxidized Ni center (Supplementary Fig. S45).[46]

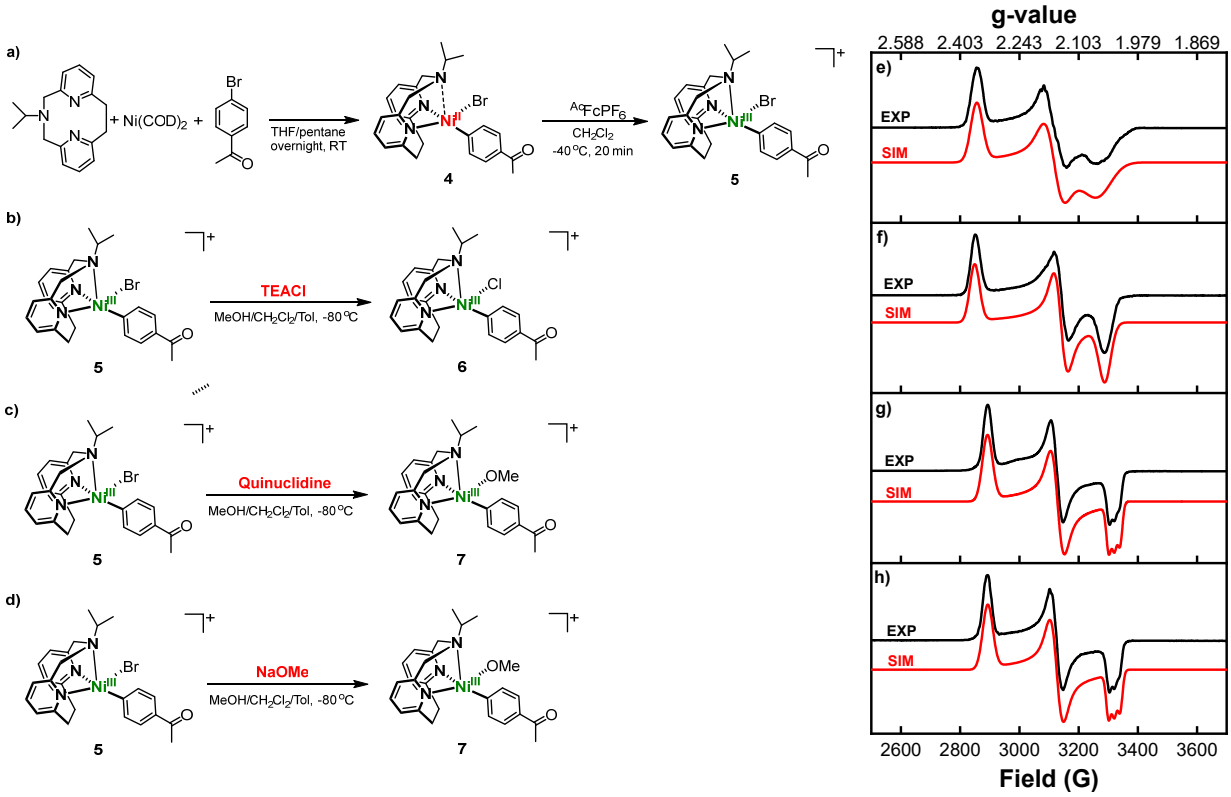

Figure 5. (left) Experimental setup for the synthesis of (^{iPr}N3)Ni^{II}(PhAc)Br (**4**) and EPR detection of (a) [(^{iPr}N3)Ni^{III}(PhAc)(Br)]$^+$ (**5**), (b) [(^{iPr}N3)Ni^{III}(PhAc)(Cl)]$^+$ (**6**), and (c and d) [(^{iPr}N3)Ni^{III}(PhAc)(OMe)]$^+$ (**7**). (right) Experimental (black) and simulated (red) EPR spectra of the reaction mixtures recorded at 77 K in 1:1:3 MeOH:CH_2Cl_2:Toluene frozen glass: (e) [(^{iPr}N3)Ni^{III}(PhAc)(Br)]$^+$ (**5**), (f) [(^{iPr}N3)Ni^{III}(PhAc)(Cl)]$^+$ (**6**), and (g and h) [(^{iPr}N3)Ni^{III}(PhAc)(OMe)]$^+$ (**7**). The following parameters were used for simulation of (e) g_x = 2.356, g_y = 2.158, g_z = 2.059; (f) g_x = 2.363, g_y = 2.144, g_z = 2.047; (g) g_x = 2.326, g_y = 2.151, g_z = 2.027 (A_z(N) = 19.4 G); (h) g_x = 2.326, g_y = 2.152, g_z = 2.027 (A_z(N) = 19.5 G).

The appreciable stability of **5** allowed us to investigate its reactivity. When **5** was reacted with 1 equiv tetraethylammonium chloride (TEACl, Fig. 5b), a rhombic EPR spectrum with g_x = 2.363, g_y = 2.144, g_z = 2.047 and sharper signals than the spectrum of **5** was obtained, indicating the likely formation of the [(^{iPr}N3)Ni^{III}(PhAc)(Cl)]$^+$ species **6** (Fig. 5f vs. Fig. 5e). A similar EPR

signal broadening due to superhyperfine coupling to the Br atom (I = 3/2) vs the Cl atom (I = 3/2) was observed in a previous study by our group, where the structural analysis of $[(^{tBu}N4)Ni^{III}Ar(X)]^+$ complexes (X = Br or Cl) confirmed the effect of the halide ligand onto the corresponding EPR spectra.[15] Importantly, an EPR spectrum resembling the proposed 6-coordinate species $(^{iPr}N3)Ni^{III}(PhAc)BrCl$ (**3**) was not observed, supporting the instability of this sterically hindered species. GC-MS analysis of the solution of **6** after warming up to room temperature in the absence of MeOH reveals Ar–Cl product formation (Supplementary Fig. S24), while the reaction between $(^{iPr}N3)Ni^{II}(PhAc)Br$ (**4**) and $PhICl_2$ generates an EPR spectrum identical to that of **6** (Supplementary Figs. S26), providing additional experimental evidence for the halide exchange step. Next, we probed the ligand exchange step with an alkoxide. The addition at –80 °C of quinuclidine in MeOH to **5** generates a species assigned as the Ni^{III}-aryl alkoxide complex $[(^{iPr}N3)Ni^{III}(PhAc)(OMe)]^+$ (**7**), which exhibits a rhombic EPR signal with g_x = 2.326, g_y = 2.151, g_z = 2.027 and superhyperfine coupling to the one axial N (I = 1) donor in the g_z direction of $A_z(N)$ = 19.4 G (Fig. 5g). We posit that replacement of the halides that exhibit superhyperfine interactions (Br or Cl, I = 3/2) by the methoxide ligand resolves the superhyperfine coupling to the N atom along the g_z direction, while the weaker π-donor methoxide leads to a stronger $Ni–N_{axial}$ interaction. The identity of **7** was further confirmed by the treatment of **5** with 1 equiv NaOMe, which generated an identical EPR spectrum (Fig. 5h and Supplementary Fig. S32). Importantly, to the best of our knowledge this is the first experimental observation of a ligand exchange reaction (either by a halide or alkoxide) occurring at a Ni^{III} metal center, which is typically proposed as a key step in Ni-mediated C-C and C-heteroatom bond formation reactions.[47,48] Finally, we also note that **5** is a catalytically competent species (Supplementary Table S8) and affords the C–O cross-

coupled product in 31% yield, suggesting that **5** can successfully enter the catalytic cycle. In this case, the lower yield is likely due to the slight decomposition of **5** in RT during the catalytic reaction.

Upon warming up to room temperature, species **6** and **7** undergo C–O bond-forming reductive elimination, affording 4-methoxyacetophenone together with different amounts of acetophenone (Fig. 6 and Supplementary Figs. S36–S41), and consistent with a favorable reductive elimination from a Ni^{III} species.[49,50] Moreover, the addition of excess anionic ligands (Cl^- or OMe^-) leads to increased yields of the C–O coupled product (Fig. 6) and faster decomposition of **6** and **7**, as seen in the fast decay of their EPR signals (Supplementary Figs. S25 and S31). We propose that coordination of an additional anionic ligand in the presence of excess base leads to the formation of a congested 6-coordinate Ni^{III} center – due to the steric hindrance of the ethylene bridge that blocks the second axial coordination site (Fig. 2d), and consequently results in accelerated C–O reductive elimination. This is also in line with the observed rapid decay of the 6-coordinate species (^{iPr}N3)Ni^{III}(PhAc)BrCl (**3** , Fig. 4c and Supplementary Fig. S20). In addition, the rapid reductive elimination from a 6-coordinate Ni^{III} center may preclude β-hydride elimination (Fig. 6, entry 6), which is likely the source of the formation of **b**. Overall, these EPR and reactivity studies provide a complete picture of the Ni^{I}/Ni^{III} catalytic cycle for the C–O cross-coupling reaction, with experimental evidence for each essential step in this process: oxidative addition, transmetalation/ligand exchange, and reductive elimination.

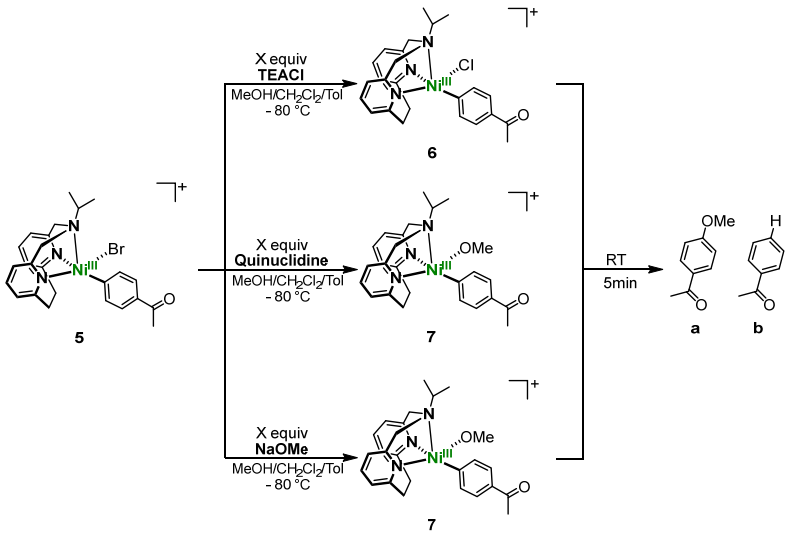

Entry	Additive equiv.	a (%)[a]	b (%)[a]
1	1 equiv. TEACl	13	20
2	10 equiv. TEACl	33	30
3	1 equiv. Quinuclidine	28	28
4	10 equiv. Quinuclidine	33	22
5	1 equiv. NaOMe	41	24
6	10 equiv. NaOMe	57	0

[a]Yields were determined using GC-FID with 1,3-benzodioxole as a standard.

Figure 6. Stoichiometric reactivity of **5** with TEACl, quinuclidine, or NaOMe to yield the C–O coupled product through reductive elimination from Ni^{III} intermediates.

Mechanistic considerations

Finally, based on the photoredox/Ni dual catalytic studies under blue LED light (Table 2), we evaluated the thermodynamic feasibility of the photocatalytic process in the C–O coupling reaction. A comparison of the redox potentials of the Ni complexes and photocatalysts implies that a reductive quenching pathway is not operating, as the observed production yields contradicts the trend of the oxidation strength of excited photocatalysts (Supplementary Information, page S27). Instead, an oxidative quenching pathway is proposed to be operative, in which the initial step is the single-electron reduction of Ni^{II} by the excited photocatalyst, and this is in line with our results

in which all photocatalysts with $E(M^+/*M) < -0.87$ V afford the C–O coupling product. By combining the insights obtained from EPR and reactivity studies and the photoredox/Ni dual catalysis, two photocatalytic mechanisms are proposed (Fig. 7). The $(^{R}N3)Ni^{II}$ complex is reduced to a Ni^{I} species either by irradiation with purple LED light (Fig. 7a) or via a single electron transfer (SET) from the excited photocatalyst (Fig. 7b), followed by an oxidative addition of the aryl halide to form a transient $(^{R}N3)Ni^{III}Ar(Br)X$ species. For both of the direct light-promoted Ni catalysis and dual Ni/photoredox catalysis, the $(^{R}N3)Ni^{III}$ species can undergo a ligand exchange with the alcohol substrate in presence of excess base to generate the $(^{R}N3)Ni^{III}Ar(OR)X$ species, which is then proposed to undergo a subsequent reductive elimination to yield the C–O coupled product and regenerate a $(^{R}N3)Ni^{I}$ species, completing the catalytic cycle. We note that light on/off experiments (Supplementary Information, page S26) support a self-sustained Ni^{I}/Ni^{III} cycle, and the requirement for intermittent light during the reaction may help to regenerate the depleted $(^{R}N3)Ni^{I}$ species. Importantly, the use of tridentate pyridinophane $^{R}N3$ ligands generates a sterically hindered 6-coordinate Ni^{III} center due to the H atoms of the ethylene bridge and that is proposed to promote a rapid reductive elimination. For the proposed dual Ni/photoredox catalysis (Fig. 7b), the $(^{R}N3)Ni^{I}$ species can directly re-enter the catalytic cycle, or it can be oxidized to the $(^{R}N3)Ni^{II}$ complex via an SET process with the oxidized photocatalyst Ir^{IV}, thus regenerating the Ir^{III} photocatalyst. Taken together, both mechanisms are proposed to involve both Ni^{I} and Ni^{III} intermediates, which are involved in the oxidation addition step, and the ligand exchange/transmetalation and reductive elimination steps, respectively. The main difference between the two pathways is the generation of the catalytically active $(^{R}N3)Ni^{I}$ species, either through light-promoted reduction of the Ni^{II} precursor (Fig. 7a), or by the excited photocatalyst

(Fig. 7b).

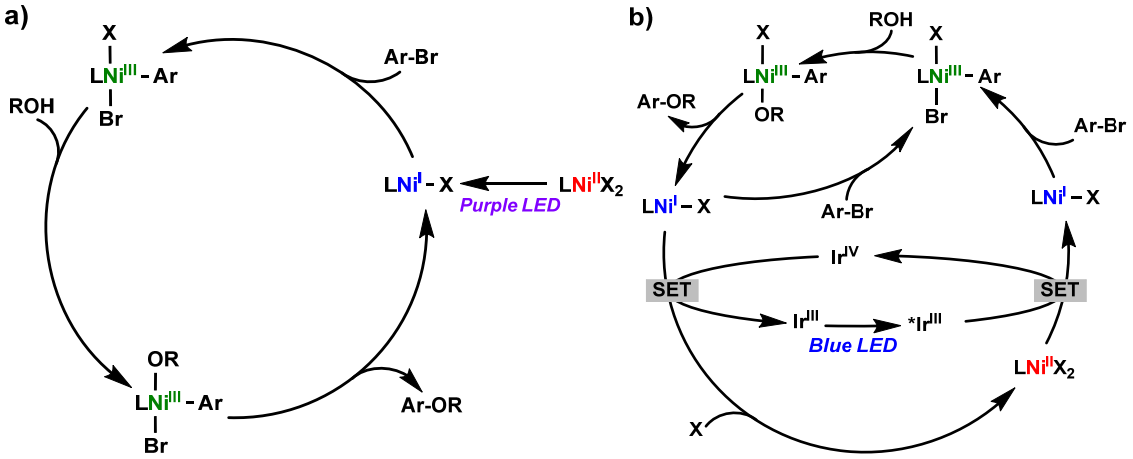

Figure 7. Proposed mechanisms for the C–O cross coupling reaction for (a) direct light-promoted Ni catalysis with purple LED light, and (b) dual Ni/photoredox catalysis with blue LED light. X = Cl or Br, L = ^{Me}N3 or ^{iPr}N3.

Conclusion

We herein report new tridentate pyridinophane ^{R}N3 ligands and their Ni complexes, which were employed in mechanistic studies of the photocatalytic C–O cross-coupling reaction. The (^{R}N3)NiCl$_2$ complexes are active photocatalysts for the C–O cross-coupling in the absence of a precious metal photocatalyst. Employing these newly developed ^{R}N3 ligands allowed us to directly probe for the first time the key steps of the C–O cross-coupling catalytic cycle involving paramagnetic Ni species: the oxidative addition of an aryl halide to a Ni^{I} species to generate a Ni^{III} species, the ligand exchange/transmetalation step at a Ni^{III} center, and the C–O bond forming reductive elimination from a Ni^{III} species. Overall, the present work suggests that the ^{R}N3 ligands can lead to the development of new Ni catalysts, and are also a practical platform for detailed

mechanistic studies of related Ni-catalyzed reactions.

Methods

General procedure for the C-O cross-coupling reaction. In a N_2-filled glovebox, 4-bromoacetophenone (0.4 mmol, 1.0 equiv), quinuclidine (0.44 mmol, 1.1 equiv), MeOH (1.6 mmol, 4 equiv), (^{Me}N3)$NiCl_2$ (2 mol%), and a magnetic stir bar were added into 0.4 mL THF in a vial. The vial was irradiated with one Kessil purple LED lamp (λ_{max} = 390 nm, max 52 W) under fan cooling. After 24 h, 1,3-benzodioxole (0.4 mmol) was added to the reaction mixture at a standard, and the reaction mixture was analyzed by ^{1}H NMR in $CDCl_3$ and GC-FID to determine the yield of C-O coupled product. Authentic 4-methoxyacetophenone was purchased from AK scientific and used to determine the retention time and response factor for GC-FID quantification.

General procedure for EPR detection of 2 and 3: In a N_2-filled glovebox, a MeOH solution of **1b** was layered on top of a frozen PrCN solution of $CoCp^*_2$ and 4-bromoacetophenone in the EPR tube. The mixture was quickly frozen and taken outside of the glove box. The reaction mixture was mixed at –95 °C, quickly frozen at 77 K, and then the sample was warmed up for ~10 s to –95 °C to allow for a complete reaction.

General procedure for EPR detection of 5, 6, and 7: In a N_2-filled glovebox, an EPR tube was charged with 1:3 CH_2Cl_2:Toluene or CH_2Cl_2:PrCN solution of **5** and frozen at 77 K. A MeOH solution of TEACl, quinuclidine, or NaOMe was added over the frozen solution of **5**. After taking out the EPR tube from the glovebox, an initial EPR spectrum was taken at 77 K (for **5**). After a quick shake of the tube for 10 s at –95 °C (for **6** or **7**), the sample was frozen at 77 K and the EPR spectrum was collected.

Data availability

Crystallographic data for the structures reported in this article have been deposited at the Cambridge Crystallographic Data Centre, under deposition numbers CCDC 2085516 (**1a**) and 2085517 (**1b**). All data generated and analyzed are included in its Supplementary Information, including synthetic details, spectroscopic and electrochemical characterization of new compounds, computational details, mechanistic studies, and X-ray crystallographic details.

Corresponding Author

Liviu M. Mirica – Department of Chemistry, University of Illinois at Urbana-Champaign, 600 S. Mathews Avenue, Urbana, IL, 61801, USA.

Email: mirica@illinois.edu

Author

Hanah Na – Department of Chemistry, University of Illinois-Urbana Champaign, 600 S. Mathews Avenue, Urbana, IL, 61801, USA.

ORCID

Liviu M. Mirica: 0000-0003-0584-9508

Hanah Na: 0000-0002-0576-4806

Acknowledgements

We thank National Science Foundation (CHE-1925751) for financial support. We also thank Leonel Griego for helpful discussions and Dr. Richard T. Haasch for the XPS analysis.

Author Contributions

L.M.M. conceived the initial ligand synthesis procedure. H.N. and L.M.M. conceived and designed the experiments, H.N. carried out the experimental work, L.M.M. performed computational calculations, and H.N. analyzed the computational and experimental data. H.N. and L.M.M. wrote the manuscript.

Competing financial interests

A provisional patent has been filed on the synthesis and applications of the tridentate pyridinophane ligands.

TOC Graphical abstract

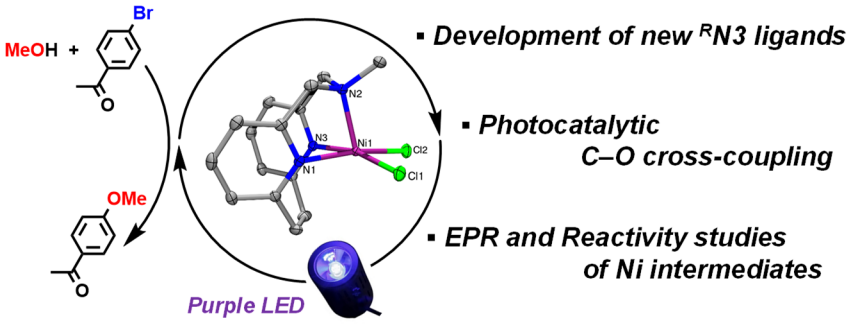

REFERENCES

1. Hartwig, J. F. Carbon-heteroatom bond formation catalysed by organometallic complexes. *Nature* **455**, 314-322 (2008).
2. Hartwig, J. F. *Organotransition Metal Chemistry: From Bonding to Catalysis* (University Science Books, 2010).
3. Meijere, A. d., Bräse, S. & Oestreich, M. *Metal Catalyzed Cross-Coupling Reactions and More*. (Wiley, New York, 2014).
4. Torraca, K. E., Huang, X. H., Parrish, C. A. & Buchwald, S. L. An efficient intermolecular palladium-catalyzed synthesis of aryl ethers. *J. Am. Chem. Soc.* **123**, 10770-10771 (2001).
5. Wu, X. X., Fors, B. P. & Buchwald, S. L. A Single Phosphine Ligand Allows Palladium-Catalyzed Intermolecular C-O Bond Formation with Secondary and Primary Alcohols. *Angew. Chem., Int. Ed.* **50**, 9943-9947 (2011).
6. Zhang, H., Ruiz-Castillo, P. & Buchwald, S. L. Palladium-Catalyzed C-O Cross-Coupling of Primary Alcohols. *Org. Lett.* **20**, 1580-1583 (2018).
7. Maligres, P. E., Li, J., Krska, S. W., Schreier, J. D. & Raheem, I. T. C-O cross-coupling of activated aryl and heteroaryl halides with aliphatic alcohols. *Angew. Chem., Int. Ed.* **51**, 9071-9074 (2012).
8. Terrett, J. A., Cuthbertson, J. D., Shurtleff, V. W. & MacMillan, D. W. C. Switching on elusive organometallic mechanisms with photoredox catalysis. *Nature* **524**, 330-334 (2015).
9. Escobar, R. A. & Johannes, J. W. A Unified and Practical Method for Carbon–Heteroatom Cross-Coupling using Nickel/Photo Dual Catalysis. *Chem. Eur. J.* **26**, 5168-5173 (2020).
10. Shields, B. J., Kudisch, B., Scholes, G. D. & Doyle, A. G. Long-Lived Charge-Transfer States of Nickel(II) Aryl Halide Complexes Facilitate Bimolecular Photoinduced Electron Transfer. *J. Am. Chem. Soc.* **140**, 3035-3039 (2018).
11. Yang, L. *et al.* Light-Promoted Nickel Catalysis: Etherification of Aryl Electrophiles with Alcohols Catalyzed by a Ni(II)-Aryl Complex. *Angew. Chem., Int. Ed.* **59**, 12714-12719 (2020).
12. Diccianni, J. B. & Diao, T. Mechanisms of Nickel-Catalyzed Cross-Coupling Reactions. *Trends Chem.* **1**, 830-844 (2019).
13. Sun, R. *et al.* Elucidation of a Redox-Mediated Reaction Cycle for Nickel-Catalyzed Cross Coupling. *J. Am. Chem. Soc.* **141**, 89-93 (2019).
14. Sun, R., Qin, Y. & Nocera, D. G. General Paradigm in Photoredox Nickel-Catalyzed Cross-Coupling Allows for Light-Free Access to Reactivity. *Angew. Chem., Int. Ed.* **59**, 9527-9533 (2020).
15. Zheng, B. *et al.* Organometallic Nickel(III) Complexes Relevant to Cross-Coupling and Carbon-Heteroatom Bond Formation Reactions. *J. Am. Chem. Soc.* **136**, 6499-6504 (2014).
16. Zhou, W., Zheng, S. A., Schultz, J. W., Rath, N. P. & Mirica, L. M. Aromatic Cyanoalkylation

through Double C-H Activation Mediated by Ni(III). *J. Am. Chem. Soc.* **138**, 5777-5780 (2016).
17. Schultz, J. W., Fuchigami, K., Zheng, B., Rath, N. P. & Mirica, L. M. Isolated Organometallic Nickel(III) and Nickel(IV) Complexes Relevant to Carbon-Carbon Bond Formation Reactions. *J. Am. Chem. Soc.* **138**, 12928–12934 (2016).
18. Smith, S. M., Rath, N. P. & Mirica, L. M. Axial Donor Effects on Oxidatively Induced Ethane Formation from Nickel-Dimethyl Complexes. *Organometallics* **38**, 3602-3609 (2019).
19. Zhou, W., Schultz, J. W., Rath, N. P. & Mirica, L. M. Aromatic Methoxylation and Hydroxylation by Organometallic High-Valent Nickel Complexes. *J. Am. Chem. Soc.* **137**, 7604-7607 (2015).
20. Smith, S. M. *et al.* Aerobic C-C and C-O bond formation reactions mediated by high-valent nickel species. *Chem. Sci.* **10**, 10366-10372 (2019).
21. Yang, L. *et al.* Synthesis of Phenols: Organophotoredox/Nickel Dual Catalytic Hydroxylation of Aryl Halides with Water. *Angew. Chem., Int. Ed.* **57**, 1968-1972 (2018).
22. Camasso, N. M. & Sanford, M. S. Design, synthesis, and carbon-heteroatom coupling reactions of organometallic nickel(IV) complexes. *Science* **347**, 1218-1220 (2015).
23. Roberts, C. C., Camasso, N. M., Bowes, E. G. & Sanford, M. S. Impact of Oxidation State on Reactivity and Selectivity Differences between Nickel(III) and Nickel(IV) Alkyl Complexes. *Angew. Chem., Int. Ed.* **58**, 9104-9108 (2019).
24. Watson, M. B., Rath, N. P. & Mirica, L. M. Oxidative C-C Bond Formation Reactivity of Organometallic Ni(II), Ni(III), and Ni(IV) Complexes. *J. Am. Chem. Soc.* **139**, 35-38 (2017).
25. Overberger, C. G., Lombardino, J. G. & Hiskey, R. G. Novel Reductions of N-Nitrosodibenzylamines—A New Reaction1. *J. Am. Chem. Soc.* **80**, 3009-3012 (1958).
26. Takemura, H., Shinmyozu, T. & Inazu, T. A new synthetic method of [2.2]cyclophanes. *Tetrahedron Lett.* **29**, 1031-1032 (1988).
27. Wessel, A. J., Schultz, J. W., Tang, F., Duan, H. & Mirica, L. M. Improved synthesis of symmetrically & asymmetrically N-substituted pyridinophane derivatives. *Org. Biomol. Chem.* **15**, 9923-9931 (2017).
28. Kennedy, S. H., Dherange, B. D., Berger, K. J. & Levin, M. D. Skeletal editing through direct nitrogen deletion of secondary amines. *Nature* **593**, 223-227 (2021).
29. Addison, A. W., Rao, T. N., Reedijk, J., van Rijn, J. & Verschoor, G. C. Synthesis, structure, and spectroscopic properties of copper(II) compounds containing nitrogen-sulphur donor ligands; the crystal and molecular structure of aqua[1,7-bis(N-methylbenzimidazol-2[prime or minute]-yl)-2,6-dithiaheptane]copper(II) perchlorate. *J. Chem. Soc., Dalton Trans.*, 1349-1356 (1984).
30. Khusnutdinova, J. R., Luo, J., Rath, N. P. & Mirica, L. M. Late First-Row Transition Metal Complexes of a Tetradentate Pyridinophane Ligand: Electronic Properties and Reactivity Implications. *Inorg. Chem.* **52**, 3920-3932 (2013).

31. Na, H., Watson, M. B., Tang, F., Rath, N. & Mirica, L. M. Photoreductive Chlorine Elimination from a Ni(III)Cl2 Complex Supported by a Tetradentate Pyridinophane Ligand. *Chem. Comm.*, ASAP https://doi.org/10.1039/D1CC02114A (2021).
32. Martin, R. L. Natural transition orbitals. *J. Chem. Phys.* **118**, 4775-4777 (2003).
33. Hockin, B. M., Li, C., Robertson, N. & Zysman-Colman, E. Photoredox catalysts based on earth-abundant metal complexes. *Catal. Sci. Technol.* **9**, 889-915 (2019).
34. Förster, C. & Heinze, K. Photophysics and photochemistry with Earth-abundant metals – fundamentals and concepts. *Chem. Soc. Rev.* **49**, 1057-1070 (2020).
35. Zink, J. I. Photo-induced metal–ligand bond weakening, potential surfaces, and spectra. *Coord. Chem. Rev.* **211**, 69-96 (2001).
36. Wagenknecht, P. S. & Ford, P. C. Metal centered ligand field excited states: Their roles in the design and performance of transition metal based photochemical molecular devices. *Coord. Chem. Rev.* **255**, 591-616 (2011).
37. Ting, S. I. *et al.* 3d-d Excited States of Ni(II) Complexes Relevant to Photoredox Catalysis: Spectroscopic Identification and Mechanistic Implications. *J. Am. Chem. Soc.* **142**, 5800-5810 (2020).
38. Iyoda, M., Sakaitan, M., Otsuka, H. & Oda, M. Reductive coupling of benzyl halides using nickel(0)-complex generated in situ by the presence of tetraethylammonium iodide, a simple and convenient synthesis of bibenzyls. *Chem. Lett.* **14**, 127-130 (1985).
39. Campeau, L.-C. & Hazari, N. Cross-Coupling and Related Reactions: Connecting Past Success to the Development of New Reactions for the Future. *Organometallics* **38**, 3-35 (2019).
40. Lipschutz, M. I., Yang, X., Chatterjee, R. & Tilley, T. D. A Structurally Rigid Bis(amido) Ligand Framework in Low-Coordinate Ni(I), Ni(II), and Ni(III) Analogues Provides Access to a Ni(III) Methyl Complex via Oxidative Addition. *J. Am. Chem. Soc.* **135**, 15298 (2013).
41. Inatomi, T. *et al.* Ni(I)–Ni(III) cycle in Buchwald–Hartwig amination of aryl bromide mediated by NHC-ligated Ni(I) complexes. *Catal. Sci. Technol.* **9**, 1784-1793 (2019).
42. Yamamoto, T., Wakabayashi, S. & Osakada, K. Mechanism of C-C coupling reactions of aromatic halides, promoted by Ni(COD)2 in the presence of 2,2′-bipyridine and PPh3, to give biaryls. *J. Organomet. Chem.* **428**, 223-237 (1992).
43. Yin, H. & Fu, G. C. Mechanistic Investigation of Enantioconvergent Kumada Reactions of Racemic alpha-Bromoketones Catalyzed by a Nickel/Bis(oxazoline) Complex. *J. Am. Chem. Soc.* **141**, 15433-15440 (2019).
44. Evans, D. F. Determination of the Paramagnetic Susceptibility of Substances in Solution By NMR. *J. Chem. Soc.*, 2003-2005 (1959).
45. Loliger, J. & Scheffold, R. Paramagnetic Moment Measurements by NMR - A micro technique. *J. Chem. Educ.* **49**, 646-647 (1972).
46. Colpas, G. J. *et al.* X-ray Spectroscopic Studies of Nickel Complexes, with Application to

the Structure of Nickel Sites in Hydrogenases. *Inorg. Chem.* **30**, 920-928 (1991).
47. Shields, B. J. & Doyle, A. G. Direct C(sp3)–H Cross Coupling Enabled by Catalytic Generation of Chlorine Radicals. *J. Am. Chem. Soc.* **138**, 12719-12722 (2016).
48. Sheppard, T. D. Metal-catalysed halogen exchange reactions of aryl halides. *Org. Biomol. Chem.* **7**, 1043-1052 (2009).
49. Matsunaga, P. T., Hillhouse, G. L. & Rheingold, A. L. Oxygen-Atom Transfer from Nitrous-Oxide to a Nickel Metallacycle - Synthesis, Structure, and Reactions of (2,2'-Bipyridine)Ni(OCH2CH2CH2CH2). *J. Am. Chem. Soc.* **115**, 2075-2077 (1993).
50. Han, R. Y. & Hillhouse, G. L. Carbon-oxygen reductive-elimination from nickel(II) oxametallacycles and factors that control formation of ether, aldehyde, alcohol, or ester products. *J. Am. Chem. Soc.* **119**, 8135-8136 (1997).